

Cold Gas Kinematics in an L_* Spiral Galaxy at $z = 0.437$: The Nature of Damped Lyman- α Absorbers

F.H. Briggs¹, A.G. de Bruyn^{1,2}, R.C. Vermeulen²

¹ Kapteyn Astronomical Institute, P.O. Box 800, 9700 AV Groningen, The Netherlands

² ASTRON, P.O. Box 2, 7990 AA, Dwingeloo, The Netherlands

Received ; accepted

Abstract. Westerbork Radio Synthesis Telescope observations of the redshifted 21cm line absorber against the $z_{em} = 0.871$ double lobed quasar 3C196 show that the intervening absorber is an $L \approx L_*$ spiral galaxy (3C196-G1) and that the absorbing layer of cold gas extends to radii of at least $30 h_{50}^{-1}$ kpc. The new data solve several long standing puzzles about this system by (1) discovering a second 21cm absorption feature, corresponding to absorption against the NE lobe of the background radio source and (2) spatially “resolving” the two absorption features to isolate the absorption along the two lines of sight to the opposing radio lobes. These findings resolve the disagreement in redshift between the UV metal and 21cm lines, and as well as demonstrating that the neutral layer does absorb both lobes of the background radio source. Simple kinematic models with an inclined, rotating gas disk match the observed 21cm profile and are also compatible with both the redshift and velocity spread of the absorption measured in UV resonance lines along a third, independent line of sight to the quasar nucleus and with the lack of 21cm absorption in an earlier VLBI experiment that was sensitive to opacity against the hot spot in the northern lobe. The inferred rotation speed and luminosity for the galaxy are compatible with the $z \approx 0$ Tully-Fisher Relation.

This system illustrates well how 21cm absorption against extended background radio sources is a powerful tool in determining the nature of the damped Lyman- α class of QSO absorption line system.

Key words: Galaxies: active – Galaxies: evolution – Galaxies: interaction – Radio lines: galaxies

1. Introduction

Cold neutral gas traces gravitational potential wells, and in the nearby universe, astronomers use the 21cm line as a dynamical indicator to obtain the total amount and

distribution of gravitating mass associated with galaxies. At high redshift, the neutral gas mass constitutes a larger fraction of the observable luminous mass in baryons (Lanzetta et al 1995, Storrie-Lombardi & Wolfe 2000), making the HI itself a more important gravitating element, and the stars less so. This increases the importance of selecting galaxies at high redshift based purely on their neutral gas content, since these objects are likely to point to deep gravitational potentials where the progenitors of the galaxies of the present epoch are forming.

Despite presenting different opinions on the nature of the high HI column density QSO absorption line systems with $N_{HI} \geq 2 \times 10^{20}$ atoms cm^{-2} known as “damped Lyman- α (DLa), both Prochaska & Wolfe (1998) and Haehnelt et al (1998) do agree that the DLa systems are “the progenitors of the present day normal galaxies.” Since the 21cm line requires column densities of HI in excess of $\sim 10^{20}$ atoms cm^{-2} to create strong absorption lines, the redshifted 21cm absorbers are identified with the DLa class of quasar absorption-line and thus with evolving galactic potentials.

Due to its early identification by Brown & Mitchell (1983), the 21cm line observed at $z = 0.437$ against the extended radio quasar 3C196 ($z_{em} = 0.871$) has received extensive follow-up with a variety of techniques, including ground-based and HST imaging and spectroscopy. The 3C196 line of sight has received additional attention, due to its association with DLa’s and its low redshift, which makes detection of a possible optical counterpart to the absorber and the study of the environment of the absorber easier than for the higher z DLa’s that are selected most readily in ground-based spectroscopy of the Lyman- α line at $z > 1.7$. The absorption redshift was subsequently selected in a survey for MgII absorption against steep spectrum quasars by Aldcroft et al (1993, 1994).

The optical identification of two candidates (3C196-G1 and 3C196-G2) for an intervening absorbing galaxy were made by Boissé & Boulade (1990). Subsequent HST imaging has shown that G1 is a large barred spiral located about $1.5''$ south-east of the quasar (Cohen et al 1996, Le Brun et al, 1997, Ridgway & Stockton 1997). The out-

lying spiral arms of G1 appeared to extend across the two extended radio lobes of the background radio quasar, leading to the puzzle posed by Cohen et al over why only one relatively narrow absorption profile was observed in the 21cm line spectrum, when a velocity spread of several hundred km s^{-1} would be expected for absorption over the full extent of the G1 galaxy. G2 is due north of the quasar nucleus.

A second puzzle arose from the spectroscopic studies. Ground based spectroscopy (Foltz et al 1988) showed that the metal-line absorption was spread over a wider range than the 21cm absorption, but that the redshift of the center of the metal line profiles fell at $\sim 50 \text{ km s}^{-1}$ greater than the 21cm line redshift (Cohen et al 1996).

A third important constraint comes from the spectral-line VLBI observation of Brown et al (1988), which detected no absorption against a marginally resolved hot spot in the NE radio continuum lobe and implied that the absorption must take place in a spatially extended absorber against the more diffuse and extended radio continuum structure, thus placing a lower limit on the size of the absorber of $13h_{50}^{-1} \text{ kpc}$ (Foltz et al 1998).

In summary, prior to the observations we report here, there was a candidate galaxy for which no redshift had been measured to confirm its role as the site of the 21cm absorption, and there were several puzzles about how the galaxy's kinematics might explain both the 21cm absorption profile and the line widths and redshift of the metal lines. These new 21cm line observations resolve these ambiguities, establishing the luminous barred spiral 3C196-G1 as the absorber, as well as providing a measure of its dynamical mass. The system remains an interesting candidate for high-spatial resolution radio aperture synthesis, and provides a view for how these techniques could be applied to the highest redshift DLa absorbers in order to determine their nature at much higher redshifts.

2. The WSRT Observations

New Westerbork Synthesis Radio Telescope observations were conducted in the Compound Interferometer (CI) as well as in regular synthesis mode. In the CI-mode we cross-correlate the signal from two tied-arrays each representing the summed signal of 6 telescopes (Chengalur et al 1996). In doing so we can use the full correlator capacity to record both a wide band (5 MHz) and attain high spectral resolution (15 kHz). A 12 hour observation on December 21 1996 was distributed equally between 3C196 and the bandpass calibrator source 3C147 with a duty cycle of 2 hours. The resulting spectrum is shown in Fig. 1. The 2% deep absorption line discovered by Brown & Mitchell is seen around channel 500. However, we also detected a second absorption line. This line, visible near channel 650 is both wider (about 100 km/sec) and shallower (0.3% peak absorption) [The sharp feature near channel 200 is due to interference]. No baseline was removed from the spectrum.

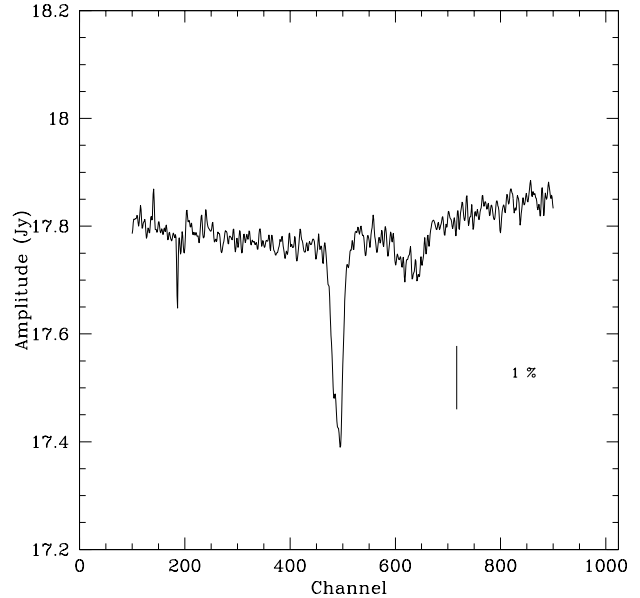


Fig. 1. Compound interferometer spectrum of 3C196. The total spectral range displayed measures about 4 MHz or 1200 km/sec . The velocity resolution is about 4.5 km sec^{-1} .

A second observation was done on January 6 1997 in regular synthesis mode using the line backend (Bos et al 1981) with 2.5 MHz and 64 channels with the central frequency halfway between the two absorption features. A total of 10 hours of integration was spent on 3C196 with the available 13 telescopes. The calibrator 3C147 was observed for a total of 3 hours before and midway during the 3C196 observation. Following a selfcalibration on 3C147 we transferred the complex passbands, on a telescope by telescope basis, to the visibilities of 3C196. The data were then Fourier transformed to yield a cube of 56 images (channels 3-58). 3C196 is unresolved by the WSRT synthesized beam at 988 MHz, which has half-power full-width of $20'' \times 26''$, and we therefore determined the peak amplitude of the source as a function of frequency. The resulting spectrum is shown in Fig. 2. No baseline had to be removed. The quality of the spectrum is indeed excellent. Both absorption features are seen with high S/N and there is no doubt about the reality of the shallower feature at 988.0 MHz. We note this because this feature was not seen in the spectrum reported by Brown & Mitchell. The superior baseline stability of interferometers compared to those obtained using a single dish is obvious. The pass-band is stable to better than one part in a thousand and is in fact limited by thermal noise in the 3C196 and 3C147 data.

The redshift measured for the optical and UV lines (Foltz et al 1988) falls between the two 21cm absorption features.

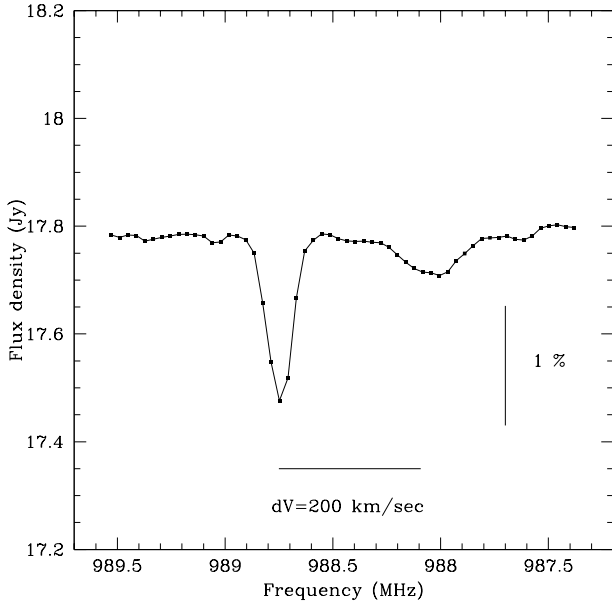


Fig. 2. Regular synthesis mode spectrum of 3C196. The spectral resolution is about 24 km sec^{-1} .

The WSRT synthesized beam at this frequency is $\sim 25''$, and this is much larger than the size of the radio source. However, the spectral dynamic range of the data, in amplitude as well as in phase, is so good ($\sim 4000:1$) that we should be able to determine the centroid of the source as a function of frequency to 1 part in 8000 of the synthesized beamwidth. This is done with the NEWSTAR program NMODEL that fits a model to the UV data. Fig. 3 shows the derived source centroid position as a function of frequency. Note that the angular scale is measured in milli-arcseconds. In three groups of continuum channels outside the absorption lines, the centroid position is found to be independent of frequency to within a few mas, as could be expected on the basis of the S/N ratio. This centroid lies about halfway between the two radiolobes. However, in the absorption channels we see a systematic shift of the source centroid. In the channels corresponding to the deepest absorption feature the source centroid shifts by about $0.040''$ to the north-east with the largest shift occurring in the channels where the absorption line reaches its lowest value of about -1.6% . Correcting the observed shift by the channel dependent depth of the absorption line, we can deduce the true location of the deep absorption feature to lie about $2.5'' \approx 0.040/0.016$ in the opposite direction, i.e. toward the south-west. This is precisely the location of the brightest hotspot relative to the continuum centroid as deduced from published 408 and 1666 MHz MERLIN images (Lonsdale & Morison 1983). The true depth of the absorption line against that hotspot must be about 4% since this hotspot is responsible for nearly 50% of the total flux density at 988 MHz.

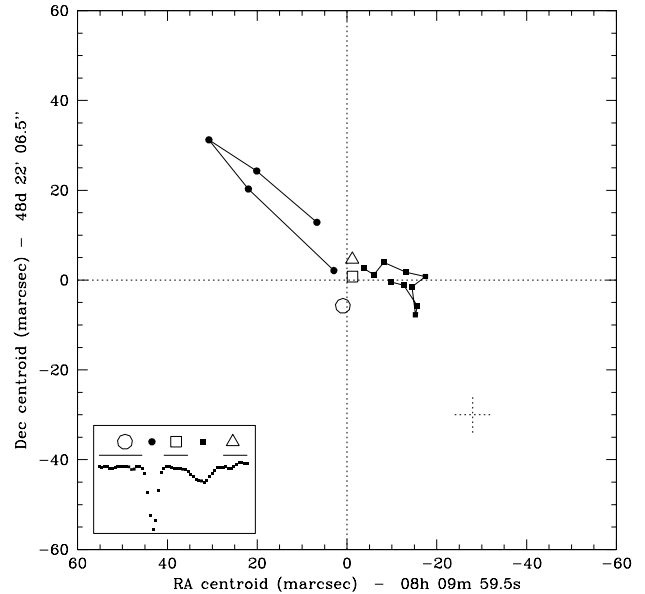


Fig. 3. Centroid position of 3C196 as a function of frequency. Note that the scale is in milli-arcseconds. For the deep and shallow absorption features five, respectively, ten channels are shown. The code for the frequency is shown at the lower left. The 1 sigma error bar per channel (4 mas) is shown by the dotted cross. The symbols for the three continuum ranges are averages over about 17, 10 and 11 channels respectively, and have a much smaller error.

The shallow absorption feature, on the other hand, shows an average centroid shift of about $0.015''$ in the opposite direction implying that the absorbed part of the radio source lies about $3.7'' \approx .015/.04$ east-north-east of the continuum centroid. This corresponds to the location of the eastern lobe of 3C196. The larger velocity width of this line suggests that gas with a range of velocities is present in front of this extended lobe. Since the total flux in this lobe (at 988 MHz) is about 15-20% of the total continuum flux the optical depth must be at least 2% and probably several times larger since gas at a single velocity will be covered by only part of the lobe. The location of the absorbing gas leaves no doubt that the barred spiral seen in the HST image is responsible for the 21cm absorption.

3. Modeling

A simple kinematic model consisting of a differentially rotating flat disk of neutral gas can explain the observational results of Figs. 1-3. We make use of the HST image in Fig. 4 (kindly provided by S. Ridgway) to locate the center and approximate orientation of the optically emitting galaxy, thereby imposing additional constraints on the geometry of the model. The UV resonance line spectroscopy against the QSO nucleus, both from ground-based telescopes and from HST, provides kinematical information

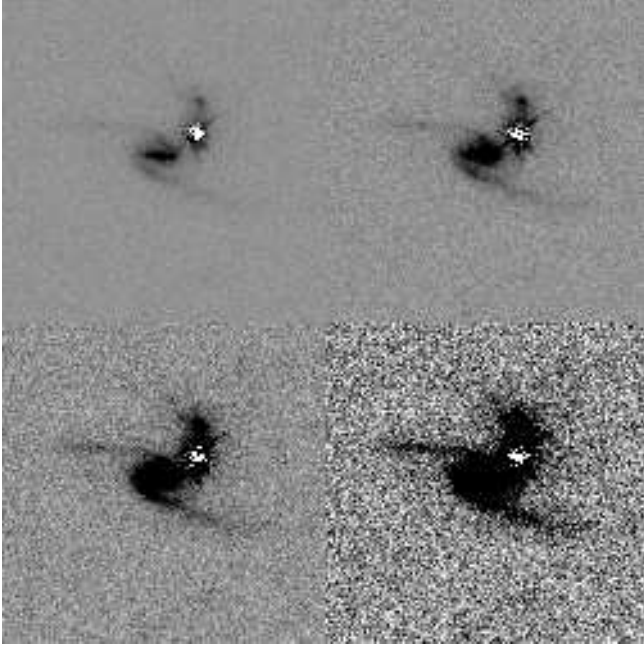


Fig. 4. HST image of 3C196 after PSF subtraction (Ridgway & Stockton 1997) shown for four contrasts.

along an additional line of sight through the galaxy. For this illustrative model, we assume a uniform gas distribution throughout the disk; the HST image shows a barred galaxy with prominent arms, which is unlikely to provide uniform optical depth. The data at hand does not justify a more detailed model.

The modeling constrains the range of galaxy model parameters but does not produce a unique fit. In exploring the parameter space, we have adjusted the following eight parameters: the offset of the galaxy center ΔRA (measured eastward) and ΔDec with respect to the origin defined in the 1666 MHz maps of Lonsdale & Morison (1983), R_{21} radius of the gaseous absorber, i inclination of the rotating disk, pa position angle of the receding side of disk major axis, V_{rot} rotation speed for a flat rotation curve, τ_{21} 21cm line optical depth measured perpendicular to the disk, and σ_{21} velocity dispersion of the gas. The parameters for four examples are listed in Table 1, along with derived quantities describing $N_{los}(HI)$ the line of sight neutral hydrogen column density ($N_{los}(HI) = 1.82 \times 10^{18} \sigma_{21} \tau_{21} T_s / \cos i$, where a spin temperature $T_s = 100$ K is adopted for these estimates), inferred M_{HI} neutral hydrogen mass within R_{21} , $M_{dyn} = V_{rot}^2 R_{21} G^{-1}$ the dynamical mass and the M_{dyn}/L_B ratio of dynamical mass to optical B-band luminosity. The derived parameters are discussed in more detail in Sect. 4.

The sizes and orientations of the absorbing disk models are illustrated in Fig. 5 by overlaying the outer boundaries of the disks on the contours of radio brightness. There is overall excellent agreement among the radio continuum

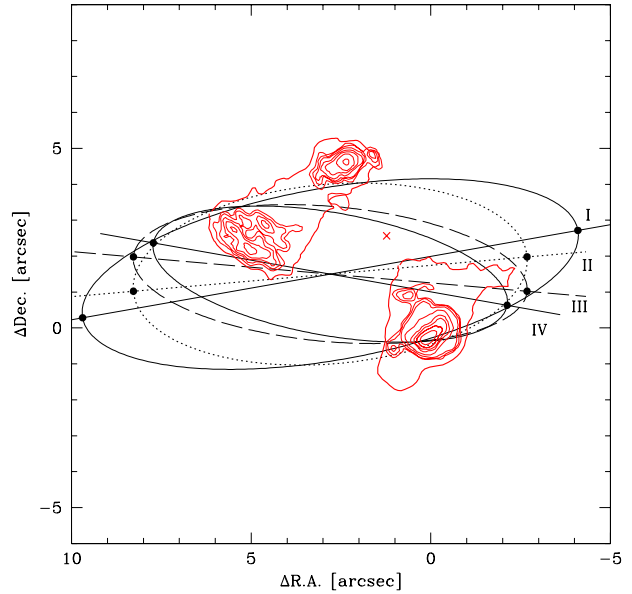


Fig. 5. Orientations and sizes of the four disk models overlaid on radio continuum contours. The representative models are labeled (I, II, III, IV) next to their major axes. The outer radio contour is taken from the 5 GHz map of Oren as shown by Cohen et al (1996); the higher contours are 1666 MHz MERLIN data from Lonsdale & Morison (1983). The position of the optical quasar and radio nucleus is marked with an \times .

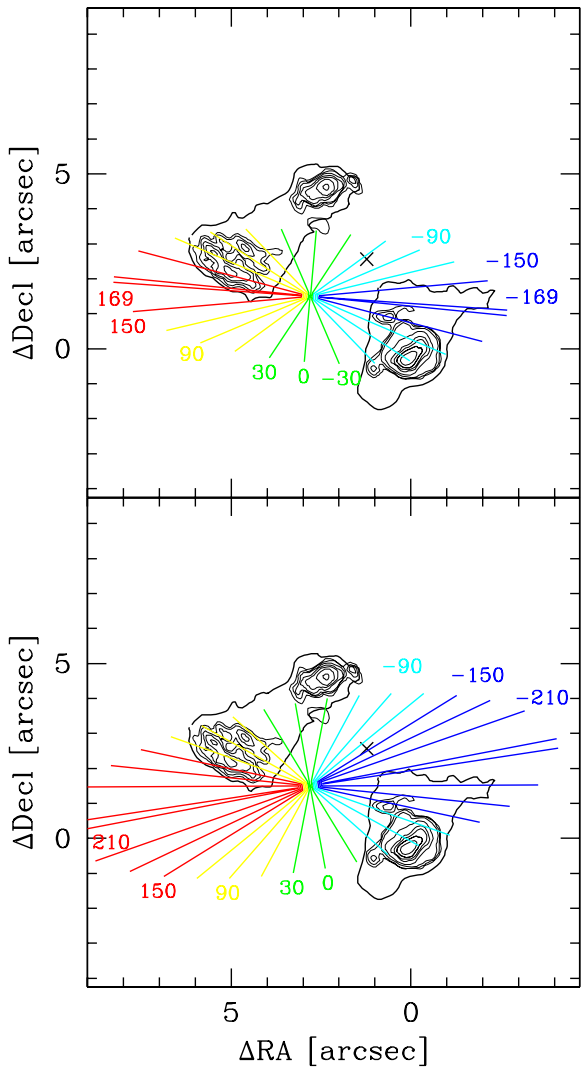
maps for 3C196, including the 408 and 1666 MHz MERLIN maps of Lonsdale & Morison (1983), the 5 GHz maps of Brown et al (1986), Lonsdale (1984), and Oren (1996, shown in Cohen et al 1996). Here, we have chosen to illustrate the structure with the 1666 MHz contours, which are the closest in $\log \nu$ to the redshifted line frequency at 988 MHz. Since the MERLIN maps lack surface brightness sensitivity for weak extended emission, we have drawn as the lowest contour the outermost VLA 5 GHz contour of Oren, which has comparable resolution to the 1666 MERLIN map. The bulk of the flux density is contained in the 1666 MHz structure, so the distribution of source intensity used for computing model absorption profiles uses purely the 1666 MHz MERLIN map. The origin of the $x-y$ coordinate system (aligned EW and NS on the sky) is located at the S-W hot spot in the S-W radio continuum lobe. In this system, the quasar nucleus is located at $+1.23''$, $+2.56''$.

Fig. 6 illustrates the velocity fields for the flat rotation curve models I and III from Table 1. The absorption spectra $S(V)$ are computed by integrating the continuum source intensity, $I(\mathbf{r}) = I(x, y)$, attenuated by the velocity dependent absorption, $\exp(-\tau_{21}(V, \mathbf{r})/\cos i)$, over the extent of the continuum source:

$$S(V) = \int_{\text{all } \mathbf{r}} e^{-\tau_{21}(V, \mathbf{r})/\cos i} I(\mathbf{r}) d\mathbf{r}$$

Table 1. Uniform Disk Models

Model		Center		p.a. pa [deg]	Radius		Incl. i [deg]	V_{rot} [km s $^{-1}$]	τ_{21}	σ_{21} [km s $^{-1}$]	$N_{\text{los}}(HI)$ ($T_s = 100$) [cm $^{-2}$]	M_{HI} $10^9 M_{\odot}$	M_{dyn} $10^{11} M_{\odot}$	$\frac{M_{\text{dyn}}}{L_{\text{B}}}$
		ΔRA [$''$]	ΔDec [$''$]		R_{21} [kpc]									$\frac{M_{\odot}}{L_{\odot}}$
I	fast	2.8	1.5	-80	7.0	52	70	250	0.06	7	$5.6(10^{20})$	13.3	7.6	14
II	Cohen	2.8	1.5	-85	5.5	41	63	250	0.03	7	$2.1(10^{20})$	4.0	6.0	11
III	slow	2.8	1.5	-95	5.5	41	70	180	0.06	7	$5.6(10^{20})$	8.2	3.1	6
IV	slow	2.8	1.5	-100	5.0	37	70	180	0.06	7	$5.6(10^{20})$	6.7	2.8	5

**Fig. 6.** The model velocity fields for models I (lower) and III (upper) overlaid on the radio continuum contours from Fig. 5.

Here, \mathbf{r} is the position vector measured in the plane of the sky relative to the x - y coordinate system defined in Fig. 5: $\mathbf{r} = x\hat{\mathbf{i}} + y\hat{\mathbf{j}}$.

The source centroid $\mathbf{r}_c(V)$ as a function of velocity results from

$$\mathbf{r}_c(V) = [S(V)]^{-1} \int_{\text{all } \mathbf{r}} \mathbf{r} e^{-\tau_{21}(V, \mathbf{r}) / \cos i} I(\mathbf{r}) d\mathbf{r}$$

The HST and ground-based optical imaging provides some constraints on the size, location and orientation of the disk model. Here, we begin by centering the absorbing disk on the galaxy tentatively identified by Boissé & Boulade (1990), Cohen et al (1996) and Le Brun et al (1997), and we conclude that the model satisfactorily explains the double-featured, 21cm line profile (in accord with the prediction of Cohen et al) as well as the velocity dependent centroid shift shown in Fig. 3. In the x - y coordinate system adopted here, the galaxy center is located at $+2.8''$, $+1.5''$. All models in Table 1 have orientations and extents that encompass the full extent of the spiral arms. Fig. 7 shows the 4 ovals defined by models I-IV overlaid on the HST image of Ridgway & Stockton (1997); we chose this image for comparison, due to its high contrast and ease of access through the online ADS database. Ridgway & Stockton have subtracted a stellar point-spread function to remove the bright QSO nucleus, and they discuss the possible connection between some of the remaining nebulosity and the QSO itself at $z_{em} = 0.871$. Here, we concentrate on the nature of the intervening spiral galaxy 3C196-G1 to the south-east of the QSO nucleus.

Since the models define a disk orientation, it is straightforward to deproject the galaxy images to view the galaxy as though it were face-on. The four images, deprojected using the model parameters in Table 1, are shown in Fig. 8.

The model spectra for the four models are shown in Fig. 9. The double-featured absorption profile is a natural consequence of the absorbing disk covering two distinct lobes of the background continuum source. In these models, the shapes of the two individual profiles depend on the distribution of continuum intensity behind the velocity gradient of the differentially rotating, disk absorption.

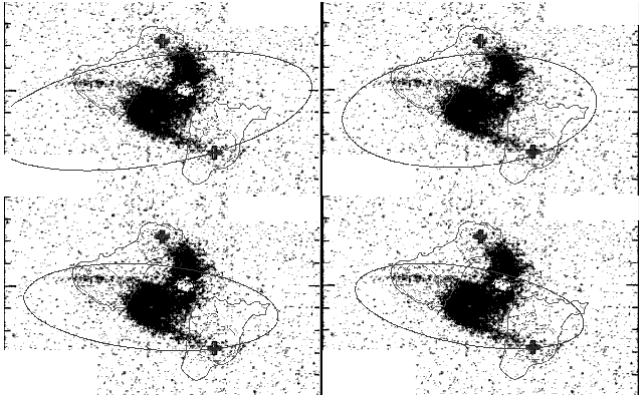


Fig. 7. The ovals representing the four models from Fig. 5 overlaid on the HST image from Ridgway & Stockton (1997). Ovals are centered on galaxy 3C166-G1. The stellar image of the quasar nucleus has been subtracted by Ridgway & Stockton. Upper row shows models I (left) and II (right); lower row has III (left) and IV (right). Crosses indicate the locations of the hot spots in the radio lobes.

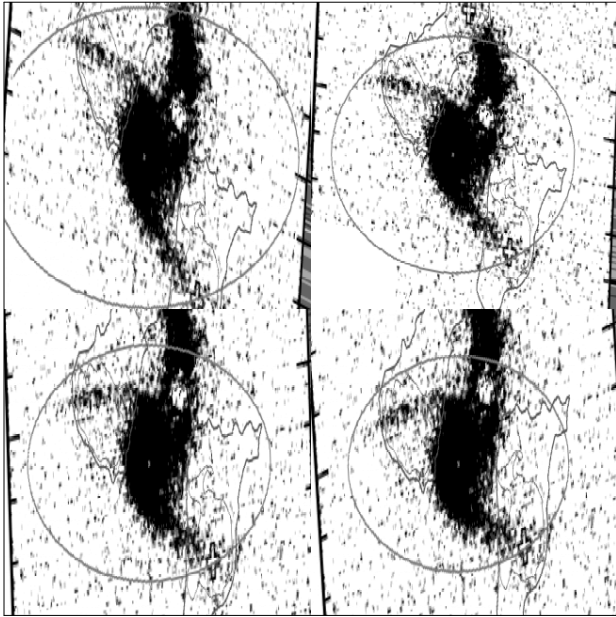


Fig. 8. Deprojected views of the optical surface brightness. Optical image of Ridgway & Stockton is projected to a face-on view, using the orientation parameters determined for the kinematical models. Ovals from Fig. 7 become circular in this view. Upper row shows models I (left) and II (right); lower row has III (left) and IV (right).

No variation in the 21cm line optical depth has been put in the model, except that the disk is limited in radius to R_{21} . Models I, II and III provide good recovery of the absorption lines of Figs. 1-2. Model IV shows an example of a model that begins to fail due to the appearance of a distinct narrow feature in the low-redshift component due to

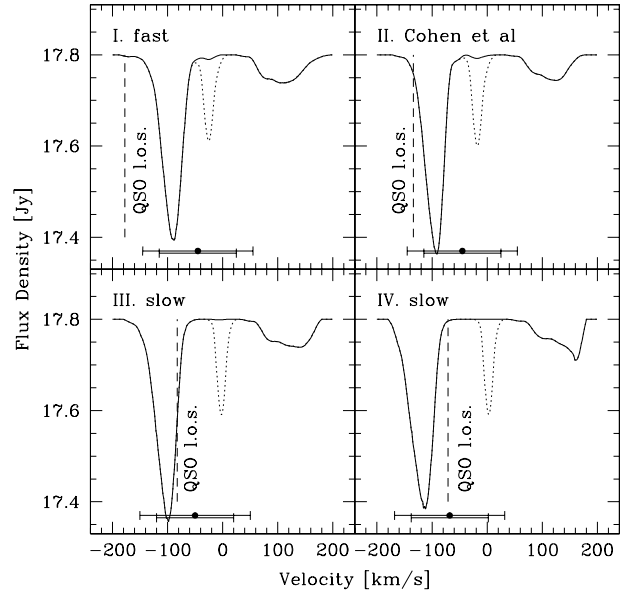


Fig. 9. Model spectra for the four representative models shown in Figs. 5-8. The model spectra are to be compared with the observed spectrum shown in Figs. (1&2). Parameters for the models are summarized in Table 1. Velocities are specified relative to the galaxy systemic velocity. The light dashed curve indicating a narrow absorption feature near the center of the profile demonstrates how the spectrum would be influenced by a disk that extends north to cover the northern lobe hotspot. The vertical dashed line represents the velocity predicted by the model for the line of sight to the quasar nucleus. The error bars indicate the FWHM velocity range of the UV/optical lines, measured for the MgII, FeII lines (wider range) and the MgI, CaII lines (narrower range); the resonance lines are positioned 50 km s^{-1} higher in redshift than the stronger component of 21cm line absorption (Cohen et al 1996).

the placement of the major axis (a region of the velocity field with low velocity gradient) over the diffuse eastern continuum lobe, leading to a feature that is akin to the horn of an inclined spiral galaxy emission profile.

Fig. 9 further shows that the spectral shape imposes a limit on the diameter and inclination of the model disk, since any model that causes the disk to cover the bright northern hot spot would lead to the appearance of a third absorption feature.

The disk models also predict the line of sight velocity toward the quasar nucleus. This value is plotted in each panel of Fig. 9. The average value for the narrow resonance line absorption lies between the components of the double-featured 21cm line profile, as indicated in the figure by the point with error bars at the bottom of each panel. In this diagram, the error bars actually specify the full-width at half-maximum of the resonance line absorption measured

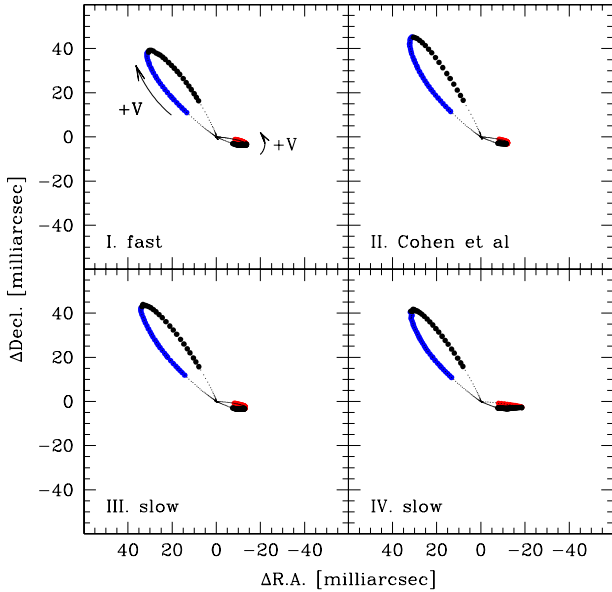


Fig. 10. Model calculations of the spectral dependence of the source centroid for the four representative models. The unabsorbed (17.8 Jy) continuum source centroid is located at the origin (0, 0) of the plot. The excursions to the NE (in the deeper absorption feature) are given large markers when the line becomes deeper than 0.15 Jy; to the East (shallow broad feature), large markers are used when the depth exceeds 0.04 Jy. The plots are to be compared with observations in Fig. 3.

by Foltz, Chaffee & Wolfe (1988); in order to account for the wide velocity spread of the metal lines, there needs to be a “turbulent medium,” probably composed of multiple, low column density clouds spread over more than 100 km s^{-1} . Such a medium may mask the presence of a cold, higher column density absorber at the velocity where the line of sight penetrates the extrapolation of the intervening galaxy disk. These separate components might be deciphered in a high spectral resolution observation of low oscillator strength metal line transitions, permitting a better separation of an extended, cold disk component from the turbulent component.

Fig. 10 indicates the location of the source centroid as a function of frequency through the 21cm line profile for comparison with Fig. (3). All models that produce reasonable “integrated absorption” profiles also lead to acceptable trajectories for the source centroid.

4. Discussion of Models

There are several considerations when appraising the models for the kinematics of 3C196-G1. The new 21cm line spectra showing the double-feature profile spread over $\sim 300 \text{ km s}^{-1}$ places the new constraints on the physical extent of the absorbing layer and the kinematics of

the gas, and, along with the self-consistent centroid shift, these facts confirm that 3C196-G1 is indeed the cause of the 21cm/damped Lyman- α absorption. It is also of great interest to understand the nature of the metal-line absorption along the line of sight to the optical nucleus of 3C196, and a satisfactory interpretation of the morphology in the HST image would be a useful outcome. Is it possible to deduce a viewing angle that allows the galaxy to be de-projected to resemble a normal barred spiral with gently winding arms, or must the galaxy’s morphology be a result of tidal interaction, possibly caused by 3C196-G2?

We first consider the advantages and disadvantages of each of the representative kinematic models in turn:

Model I does well at reproducing the 21cm absorption profiles. This model has a high rotation speed $V_{rot} = 250 \text{ km s}^{-1}$, and it is oriented (see Fig. 6) with the kinematic major axis lying closer to the line of sight to the quasar than to the hot spot in the SW radio continuum lobe. This leads to the prediction that the interception velocity towards the QSO nucleus will be blue shifted with respect to the deep 21 cm feature, in contradiction to what is observed.

Model II adopts the orientation and inclination deduced for the central stellar body of G1 by Cohen et al (1996). In our kinematic model, the radial extent of the disk is increased to cover the background radio continuum lobes with pa and i fixed at the values of Cohen et al. For this model, the interception velocity on the line of sight to the QSO nucleus falls outside the 21 cm profile, but not as greatly blue shifted as for Model I. The predicted optical/UV velocity falls at the ends of the error bars indicating the measured UV line velocity spread, implying that high spectral resolution optical observations could provide a significant test of the viability of this model.

Model III does nicely on most of the observational tests. It produces the correct velocity spread, and the galaxy’s optical morphology shows winding spiral arms. Since the line of sight to the quasar optical nucleus is closer to the minor axis of the orbits than is the hot spot in the SW continuum lobe, the predicted velocity component for the interception of the disk lies on the low redshift side of the deep 21cm feature, instead of the high redshift side. This may not be a serious problem since the disk interception velocity does lie just at one end of the FWHM velocity spread of the metal lines, and, in these sorts of MgII/FeII lines, the turbulent width is actually built up from many narrower components that represent individual absorbing clouds. Furthermore, it is expected that point-like interceptions of differentially rotating disks that are either thick or located within a corotating halo of cloudlets will produce asymmetric metal-line profiles – with the 21cm line or thickest, cold component at one side of the profile (Briggs et al 1985, Lanzetta & Bowen 1992, Prochaska & Wolfe 1997, 1998).

Model IV is minor re-orientation of model III with the goal of increasing the degree of winding of the arms in

the deprojected image and decreasing the radial extent of the gas (see Fig. 8). This relatively small change from model III produces distortion in the low redshift 21cm feature due to rotation of the major axis of the rotating disk onto the more intense part of the diffuse eastern lobe. The narrow feature that develops is the beginning of a “horn” of a conventional double-horned emission profile observed in $z = 0$ disk galaxies. This model IV has a near perfect agreement between the observed metal-line redshift and the disk interception velocity.

We have adopted models I and III for working hypotheses in the subsequent discussions, since they represent the extremes in rotation velocity while still yielding reasonable velocity profiles. However, there clearly are variations of these models, such as non-planar and non-circular motions (warps, tidally induced arms, etc) and non-uniform gas coverage that would add many additional degrees of freedom to any model that strives to fit the absorption profiles exactly. The strongest constraints are that the rotation velocity must be at least $\sim 150 \text{ km s}^{-1}$ and that the velocity field is centered on the galaxy G1. Larger rotation speeds can always be compensated to some extent by lowering the inclination i and adjusting the optical depth coverage to reproduce the observed profiles. However, the inclination cannot be lowered much from the tabulated values before the bright continuum hot-spot in the NE lobe becomes covered, which would add an additional strong absorption component to the model profiles. The uniform disk models I and III would reach the NE hot spot when i is reduced from 70° to 65° and 50° , respectively. For these models to still provide the observed velocity spread as the inclination is lowered, the disk rotation speed would have to increase by 4% for model I and 22% for model III.

The sharp edge at R_{21} assumed in the simple uniform disk model is unlikely to be realistic, and these data are unable to address the question of whether there is a hole in the neutral gas at the center of the galaxy where the bright stellar body is located. One of the most viable alternatives to the simple uniform disk model involves a tidal interaction, which would give rise to long gas-rich arms that could extend nearly radially from the host galaxy and could be highly non-planar. One possibility is that the galaxy G2 (located slightly to the north and east of the quasar nucleus) is interacting with G1, although other investigations favor the association of G2 with the quasar at $z_{em} = 0.871$ (Ridgway & Stockton 1997).

All of the disk models in Table 1 are consistent with Brown et al (1988) 988 MHz spectral-line VLBI result, which found no trace of 21cm absorption against the northeastern radio-lobe hot spot, since all the models in Table 1 cut off at radii that do not reach the hot spot. A tidal arm model would similarly place no absorbing gas over the hot spot. However, if the second galaxy G2 is actually a perturber of G1, it may be useful to observe a still broader spectrum in the 21cm line to test whether G2 has a low-level gaseous envelope that extends to the hot spot.

The line of sight column density of HI is $2.1 \times 10^{20} \text{ cm}^{-2}$ for model II and $5.6 \times 10^{20} \text{ cm}^{-2}$ for models I, III and IV. Spin temperatures in redshifted absorption systems are generally higher than the $T_s = 100 \text{ K}$ that we have adopted here (Wolfe & Davis 1979, Wolfe et al 1985, Taramopoulos et al 1995, Carilli et al 1996, Briggs et al 1997, Chengalur & Kanekar 2000), implying that the N_{HI} may be considerably higher and that this system definitely lies in the DLa class. Cohen et al (1996) measured the Lyman- α line in an HST spectrum, but they discovered that this region of the spectrum was confused by the higher order Lyman-series lines of a higher redshift Lyman-limit system at $\sim z_{em}$ and metal absorption lines. Their analysis is compatible with a range for $N_{los}(HI)$ of 2.7×10^{19} to $1.5 \times 10^{20} \text{ cm}^{-2}$, with a best-fit favoring the highest value. Thus, the preferred value of Cohen et al is in reasonable agreement with the range of column densities required in our models. The agreement provides evidence that the HI in the galaxy is distributed throughout a disk, and not concentrated solely in the strong arms that must dominate in the radio absorption spectrum, since the HST image shows the arms covering the significant areas of the radio lobes.

In the future, the models could be further constrained by synthesis mapping of the 21cm absorption system at $\sim 0.5''$ resolution. There is significant low level extended, steep spectrum radio emission that would allow a sensitive observation to map absorption by a substantial portion of the outlying gas.

The comparison of dynamical mass to luminosity for the galaxy 3C196-G1 is straightforward. Cohen et al (1996) derived a rest-frame B-band absolute magnitude of M_B of -21.3 with Hubble Constant of $H_o = 50 \text{ km s}^{-1} \text{ Mpc}^{-1}$. This point, adjusted to $H_o = 65 \text{ km s}^{-1} \text{ Mpc}^{-1}$ is plotted on the Tully-Fisher Relation of Watanabe et al (1998) in Fig. 11 using the spread in V_{rot} from 180 to 250 km s^{-1} . The range as plotted is consistent with the scatter of the local Tully-Fisher calibrators, although no corrections for extinction have been applied to the M_B measurement, making it a lower limit to optical luminosity.

5. Conclusion

The location of the absorbing gas leaves no doubt that the barred spiral seen in the HST image is responsible for the 21cm absorption. The western hotspot and eastern lobe of 3C196 are located exactly on top of spiral arm-like features emanating from the main body of the galaxy. The total velocity spread is about 250 km/sec, consistent with that expected from a massive spiral galaxy at moderate inclination. The implied column density of HI gas, for an adopted spin temperature of the HI of 100 K, is then about $10^{21} \text{ atoms cm}^{-2}$. This shows that we are dealing with a very gas rich spiral with a projected dimension of at least $6''$ or 40 kpc and a total amount of $10^{10} M_\odot$ of HI.

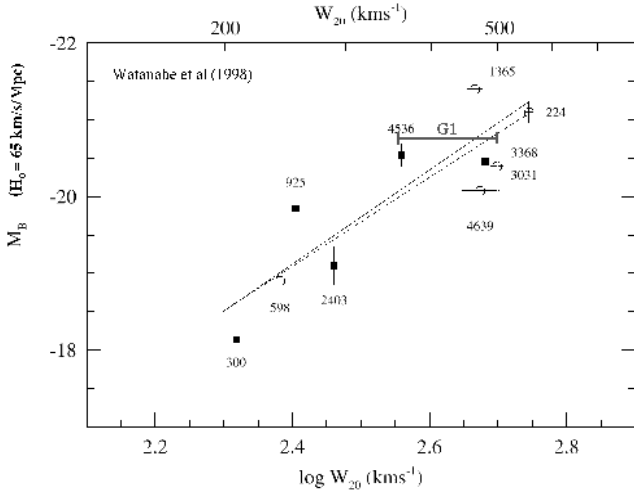


Fig. 11. Tully-Fisher Relation. Absolute B-band magnitude is plotted as a function of galaxy velocity width (here taken to be $W = 2V_{rot}$). An error bar representing galaxy 3C196-G1 is plotted on the graph of Watanabe et al (1998). Length of the bar represents the range of V_{rot} for the models I-IV. Absolute magnitude for G1 is the rest frame B-band value from Cohen et al (1996) corrected to a Hubble constant of $65 \text{ km s}^{-1} \text{ Mpc}^{-1}$.

This result shows that HI absorption study of extended, cosmologically distant, radio sources is an excellent method to probe the spatial distribution and kinematics of disks of HI at high redshifts. The median size of high redshift radio galaxies (about 50 kpc) is ideally matched to the size of gaseous disks. However, to apply this technique to more radio sources one would like to have about 30 times better angular resolution since not all radio sources are as bright as 3C196 and the use of source centroid displacement as a function of frequency as a ‘mapping’ technique is only viable in cases of exceptionally ‘deep’ absorption lines (deep in terms of the noise level). Searches for such ‘damped Ly-alpha systems’ in high redshift radio sources are currently underway.

Acknowledgements. The authors are grateful to the staff of the Westerbork Telescope for their skill and dedication in bringing the wide-band UHF receiving systems into operation. We are grateful to S.E. Ridgway for kindly providing us with a FITS file of her fully processed HST image. The Westerbork Synthesis Radio Telescope (WSRT) is operated by the Netherlands Foundation for Research in Astronomy (NFRA) with financial support of the Netherlands Organization for Scientific Research (NWO). This research has made use of the NASA Astrophysics Data System (ADS) and the NASA/IPAC Extragalactic Database (NED) which is operated by the Jet Propulsion Laboratory, California Institute of Technology, under contract with the National Aeronautics and Space Administration.

References

Aldcroft, T.L., Bechtold, J., & Elvis, M. 1994, ApJS, 93, 1

- Aldcroft, T.L., Elvis, M., & Bechtold, J. 1993, AJ, 105, 2054
 Boissé, P., & Boulade, O. 1990, A&A, 236, 291
 Bos, A., Raimond, E., van Someren Greve, H.W. 1981, A&A, 98, 251
 Briggs, F.H., Wolfe, A.M., Turnshek, D.A., Schaeffer, J. 1985, ApJ, 293, 387
 Briggs, F.H. 1990, ApJ, 352, 15
 Briggs, F.H., Brinks, E., & Wolfe, A.M. 1997, AJ, 113, 467
 Brown, R.L., & Mitchell, K.J. 1983, ApJ, 264, 87
 Brown, R.L., Broderick, J.J., & Mitchell, K.J. 1986, ApJ, 306, 107
 Brown, R.L., Broderick, J.J., Johnston, K.J., Benson, J.M., Mitchell, K.J. Waltman, W.B. 1988, ApJ, 329, 138
 Carilli, C.L., Lane, W., de Bruyn, A.G., Braun, R., Miley, G.K. 1996, AJ, 111, 1830; 1996, AJ, 112, 1317
 Chengalur, J.N., de Bruyn, A.G., Braun, R., & Carilli, C. 1996, A radio search for high redshift HI absorption. In: M.N. Bremer & N. Malcolm (eds.), Cold Gas at High Redshift, Kluwer, Dordrecht, p. 279
 Chengalur, J.N., & Kanekar, N. 2000, MNRAS, 318, 303
 Cohen, R.D., Beaver, E.A., Diplax, A., Junkkarinen, V.T., Barlow, T.A., Lyons, R.W. 1996, ApJ 456, 132
 Foltz, C.B., Chaffee, F.H., & Wolfe, A.M. 1988, ApJ, 335, 35
 Haehnelt, M.G., Steinmetz, M., & Rauch, M. 1998, ApJ, 495, 647
 Lanzetta, K.M., & Bowen, D.V. 1992, ApJ, 391, 48
 Lanzetta, K.M., Wolfe, A.M., & Turnshek, D.A. 1995, ApJ, 440, 435
 Le Brun, V., Bergeron, J., Boissé, & Deharveng, J.M. 1997 A&A, 321, 733
 Le Brun, V., Bergeron, J., Boissé, & Deharveng, J.M. 1998 A&A, 333, 851
 Lonsdale, C.J., & Morison, I. 1983, MNRAS, 203, 833
 Lonsdale, C.J. 1984, MNRAS, 208, 545
 Oren, A.L., & Wolfe, A.M. 1995, ApJ, 445, 624
 Prochaska, J.X., & Wolfe, A.M. 1997, ApJ, 487, 73
 Prochaska, J.X., & Wolfe, A.M. 1998, ApJ, 507, 113
 Ridgway, S.E., & Stockton, A. 1997, AJ, 114, 511
 Storrie-Lombardi, L.J., & Wolfe, A.M. 2000, ApJ, 543, 552
 Taramopoulos, A., Garwood, R., Briggs, F.H., & Wolfe, A.M. 1995, AJ, 109, 480
 Watanabe, M., Ichikawa, T., Okamura, S. 1998, ApJ, 503, 553
 Wolfe, A.M., & Davis, M.M. 1979, AJ, 84, 699
 Wolfe, A.M., Briggs, F.H., Turnshek, D.A., Davis, M.M., Smith, H.E., & Cohen, R. 1985, ApJ, 295, L67